Energetics and Mechanism of the Hydrogenation of XH_n for Group IV to Group VII Elements X

Elfi Kraka,* Wenli Zou, Marek Freindorf, and Dieter Cremer*

CATCO Group, Department of Chemistry, Southern Methodist University, 3215 Daniel Ave, Dallas, Texas 75275-0314, United States

S *Supporting Information*

ABSTRACT: High-level ab initio calculations of the NESC/SOC/CCSD(T)/cc-pV5Z type (NESC, Normalized Elimination of the Small Component; SOC, spin−orbit coupling corrections using the Breit−Pauli Hamiltonian) are employed to determine the energetics of the 18 hydrogenation reactions $XH_n + H_2 \rightarrow XH_{n+1} + H$ with X = F, Cl, Br, I, O, S, Se, Te, N, P, As, Sb, Bi, C, Si, Ge, Sn, and Pb. Accurate reaction and activation enthalpies as well as the corresponding free energies are obtained by calculating vibrational, thermochemical, and entropy corrections with a cc-pVTZ basis set. Also calculated are accurate X−H bond dissociation enthalpies at 298 K. The reaction mechanism of all 18 reactions is analyzed using the unified reaction valley approach (URVA) and UMP2/6-31G(d,p) to determine each reaction valley with high accuracy (step size 0.005 to 0.03 amu$^{1/2}$ bohr). By analyzing the reaction path curvature, the mechanism can be partitioned into four to six *reaction phases*, in which the reaction complex $XH_n\cdots H_2$ undergoes specific chemical transformations. The fate of the reaction complex is determined at an early stage in the entrance channel. Curvature peaks reflect the strength of the bonds being broken or formed and provide the basis for a quantitative justification of the Hammond−Leffler postulate.

1. INTRODUCTION

The mechanism of a chemical reaction is normally analyzed by calculating the properties of reactants, products, and transition state (TS) and then trying to derive from the analysis of these stationary points mechanistic features of the reaction. There is however no guarantee that the chemical processes of a reaction, i.e., bond breaking and/or bond forming, take place at or close to the TS. Also, a reaction complex will not abruptly change its bonding framework. The reactants will prepare for the chemical processes by mutual charge polarization, charge transfer from one reactant to the other, rehybridization, spin decoupling, etc., which chemists have to understand to be able to control chemical processes. The only way to get such an understanding is to install checkpoints along the reaction path at which important properties of the reaction complex are determined, which reveal the electronic structure changes proceeding with the chemical processes. There are two problems that prevent an easy realization of such computational checks. First, there seem to exist no unique checkpoints along the reaction path, and second the reacting molecules represent a statistical ensemble that follows a multitude of paths on the potential energy surface (PES), close but not identical to the minimum energy path connecting reactants, TS, and products.

In this work, we solve the problem of unraveling the electronic structure changes of the reaction complex during a chemical reaction by defining (a) the path of the reaction complex to be investigated and (b) the control points along the path at which the electronic structure of the reaction complex is analyzed. We take snapshots of the reaction complex at these points so that its mechanistic changes during the reaction can be unraveled step by step. For this purpose, we will use the Unified Reaction Valley Approach (URVA) developed by Kraka, Cremer and co-workers,[1−5] which takes the floor-line

along the harmonic reaction valley as a representative reaction path for the mechanistic analysis. These authors have shown that the electronic structure changes are reflected by the path curvature and that curvature minima correspond to minimal structural changes whereas curvature maxima describe the chemical processes.[4−6] In this way, meaningful checkpoints along a chemical reaction path are obtained that can be used to unravel the mechanism of a chemical reaction.[7−9]

We will apply URVA to 18 hydrogenation reactions of the type

$$XH_n + H_2 \rightarrow XH_{n+1} + H \tag{1}$$

with X = F, Cl, Br, I, O, S, Se, Te, N, P, As, Sb, Bi, C, Si, Ge, Sn, and Pb. We will use the curvature of the reaction path to partition the reaction path into phases with distinct structural changes of the reaction complex, which are perfectly suited to unravel the mechanism of the 18 reactions investigated. Furthermore, we will demonstrate that there is a relationship between the curvature pattern of the reaction path and the energetics of a chemical reaction, which can be used to verify the Hammond−Leffler postulate[10,11] in a quantitative rather than just a qualitative manner. In addition to the mechanistic studies, we will determine the energetics of the 18 reactions with high accuracy utilizing state-of-the-art quantum chemical methodology.

The results of this work are presented in the following way. In section 2, the ab initio quantum chemical methods used in this work will be described. In addition, a short overview over the URVA method is provided. Results and discussion are

---

presented in section 3, whereas conclusions will be drawn in the last section.

2. COMPUTATIONAL METHODS

The mechanism of the 18 reactions presented in eq 1 was investigated using a dual level approach choosing for the calculation of the energetics of all reactions a high level and for the URVA calculations a lower level quantum chemical approach.

The energetics of the 18 reactions was determined at the CCSD(T) (Coupled Cluster with all single and double excitations including a perturbative treatment of all triple excitations[12,13]) level of theory using either restricted or unrestricted HF (Hartree−Fock) reference functions and Dunning's cc-pVTZ basis sets[14−16] for the calculation of geometries, vibrational frequencies, zero-point energies, vibrational and thermochemical corrections, and entropies for molecules and TSs. The energy calculations were repeated at the CCSD(T)/cc-pV5Z level of theory utilizing calculated CCSD(T)/cc-pVTZ geometries and vibrational corrections. For atoms with an atomic number (AN) $\geq$ 35, the Stuttgart effective core potentials (ECPs)[17] were used in connection with the cc-pVnZ-PP (n = T, 5) basis sets.[18−20] For the CCSD(T) calculations, all valence (shell n) and semicore electrons (shell n − 1) were correlated.

In all cases, spin−orbit coupling (SOC) corrections were determined using the Breit−Pauli operator, for which both the one- and two-electron spin−orbit integrals were calculated.[21] For these calculations, a DK2 (Douglas−Kroll−Hess second order) relativistically contracted ANO-RCC (Atomic Natural Orbital-relativistic core correlation) basis set with triple-ζ quality was used for Sn, Sb, Te, I, Pb, and Bi,[22] whereas DK2-relativistically contracted cc-pVTZ basis sets[23] were used for the lighter atoms. State-averaged CASSCF (complete active space self-consistent field)[24,25] calculations including a DKH2 relativistic Hamiltonian were performed for the lowest three or six (for closed-shell molecules, the three lowest singlet and three lowest triplet states) electronic states, which then were used as the basis for the state interaction approach.[21] The SOC correction was calculated as the energy difference between the ground spin−orbit state and the ground spinor state. The SOC corrections obtained in this way were added to BSSE (basis set superposition error)-corrected CCSD(T)/cc-pV5Z results.

For structures containing atoms with AN $\geq$ 35, all-electron relativistic calculations were also carried out using the Dirac-exact Normalized Elimination of the Small Component (NESC) method[26] to test the ECP results. For NESC/CCSD(T) energy, geometry, and vibrational frequency calculations, the programs recently developed by Zou et al.[27−29] were employed in connection with the Sapporo-DK-TZP-2012 basis set[30,31] for the heavy atoms with AN $\geq$ 50 (Sn, Sb, Te, I, Pb, Bi) and the Dirac contracted cc-pVTZ basis set[23] for the lighter atoms. For reasons of consistency, the correlation of electrons was adjusted to that of the ECP calculations. The NESC/CCSD(T)/cc-pVTZ results (compared to the corresponding ECP results) improved final energy differences by 0.56 (X = Br) up to 2.85 kcal/mol (Pb) where the NESC improvements for the activation energies were 0.05−0.10 kcal/mol larger (however, 3.29 kcal/mol in the case of Pb). Therefore, our final energy differences were obtained at NESC/SOC/BSSE/CCSD(T)/cc-pV5Z//NESC/CCSD(T)/cc-pVTZ or simply at NESC/SOC/CCSD(T)/cc-pV5Z. For X = halogen, we also carried out CCSDT calculations and

extrapolated to the CBS (complete basis set) limit but found that improvements are too small to justify the additional calculational costs for all 18 reactions.

The URVA method has been described previously,[1−5] and therefore only its major features are summarized here. The reaction path is calculated in mass-weighted coordinates from reactants to products using as a suitable path parameter the arc length s and calculating along the path its scalar curvature and direction, which are then analyzed with the help of either the curvature coupling coefficients $B_{\mu s}$ (for identifying energy transfer mechanisms in connection with mode selective rate enhancement) or the local mode curvature coupling coefficients A_{ns} (for identifying electronic structure changes in the reaction complex).[1,2,5] In previous work, we have demonstrated that, based on the Born−Oppenheimer approximation, the concept of the PES, and the reaction path Hamiltonian,[32] changes in the scalar curvature reflect changes in the electronic structure of the reaction complex. Large curvature peaks correspond to the chemical processes of bond breaking or forming, whereas small curvature enhancements are associated with reactant orientation, charge polarization, rehybridization, or other electronic processes.[4−6] Kraka and Cremer demonstrated that curvature minima Mn (n = 1, 2, ...) indicate minimal changes of the reaction complex, which are associated with meaningful transient structures and which can be used to elucidate the mechanism of a chemical reaction.[3−5]

The curvature minima Mn are used to partition the reaction into *reaction phases*, which stretch from one curvature minimum to the next and enclose a curvature maximum or enhancement representing a particular change of the reaction complex. The analysis of the curvature enhancements (peaks) in terms of local mode curvature coupling coefficients $A_{n,s}$ (each local mode and each $A_{n,s}$ coefficient identify an internal coordinate describing a structural unit[1,33,34]) reveals which electronic structure changes are taking place. The information obtained from the scalar curvature and its decomposition into curvature coupling coefficients is complemented by the analysis of the generalized vibrational modes and their frequencies along the reaction path. In the harmonic approximation, they span the quadratic part of the reaction valley.[1,2,32]

Statistically seen, a reaction complex can follow an infinite number of trajectories through the reaction valley. URVA takes the floor line of the harmonic reaction valley as a representative path, for which a representative reaction mechanism can be identified in terms of reaction phases supported by snapshots of the reaction complex at positions M_n and, if needed, at the curvature maxima K_n. In several cases, the transient structures of the reaction complex at M_n could be assigned to *hidden intermediates*,[4,6,9] which become real intermediates if a change in the environmental or electronic factors influencing the reaction lead to the formation of a stationary point on the PES. Similarly, *hidden transition states* have been defined.[4,6]

In this work, the reaction path and the reaction valley were calculated employing unrestricted second order Møller−Plesset perturbation (UMP2) theory[35,36] in connection with Pople's VDZ+P basis set 6-31G(d,p).[37] In all reactions, the reaction complex has to be treated as a doublet state. Spin contamination was checked at the stationary points, however not explicitly treated along the reaction path. For each reaction complex, $3N - L$ (N, number of atoms; L, number of translations and rotations) internal coordinates q_n were chosen to describe the changes of the reaction complex along the reaction path. The IRC (intrinsic reaction coordinate) path in

Table 1. Comparison of Calculated and Experimental Reaction and Activation Energies[a]

no.	X	UMP2		CCSD(T)/cc-pV5Z								exptl[b]	
		ΔE_R	ΔE^a	SOC[c]	ΔE_R	SOC[c]	ΔE^a	ΔH_R (298)	ΔH^a (298)	ΔG_R (298)	ΔG^a (298)	ΔH_R (298)	ΔH^a (298)
1	F	−30.1	8.9	0.29	−31.3	0.29	2.1	−31.6	0.3	−31.9	5.3	−32.2	<1[49,50]
2	Cl	4.1	15.0	0.83	3.3	0.83	8.8	1.3	4.8	0.4	10.8	1.1	
3	Br	28.3	33.6	3.33	18.0	3.32	19.7	15.5	16.3	14.6	22.0	16.7	
4	I	37.8	41.5	7.14	35.0	7.35	35.9	32.1	32.2	30.9	37.6	32.9	
5	O	−17.7	11.4	0.19	−15.6	0.19	5.7	−14.2	4.6	−14.1	10.9	−14.6	4 ± 0.5[51]
6	S	13.9	22.9	0.49	14.2	0.49	18.2	13.3	15.5	13.0	16.8	13.0	
7	Se	20.3	27.0	2.38	25.2	2.43	27.0	23.7	24.4	23.0	30.2	24.2	
8	Te	39.1	43.0	5.34	39.4	5.74	41.0	37.5	38.2	37.1	43.8	39.2	
9	N	−8.4	14.1	0.00	−5.7	0.00	9.5	−2.9	9.5	2.0	16.9	−3.4	8.5 ± 0.5[52]
10	P	21.5	29.6	0.00	22.0	0.00	25.0	21.6	23.4	22.6	30.3	20.3	
11	As	28.1	34.1	0.02	28.8	0.01	30.4	28.0	28.6	28.9	35.3	27.9	
12	Sb	40.2	44.3	0.09	37.3	0.08	38.1	35.8	35.9	36.0	40.0	35.3	
13	Bi	45.1	48.5	1.57	41.4	1.46	41.4	39.6	38.9	39.7	44.3		
14	C	−7.5	14.7	0.00	−2.8	0.00	11.4	−0.4	10.1	0.9	18.1	−0.85	10.9 ± 0.5[53]
15	Si	11.7	22.7	0.00	13.0	0.00	18.2	12.4	15.9	12.0	23.4	12.4	
16	Ge	17.4	25.1	0.00	20.3	0.00	23.5	19.5	21.2	21.0	28.7	20.8	
17	Sn	28.6	34.8	0.06	28.3	0.07	30.0	26.8	27.7	29.0	35.5		
18	Pb	35.0	40.0	1.56	32.1	1.89	32.5	30.6	30.4	32.0	36.8		

[a]All energy values in kcal/mol. [b]Experimental reaction enthalpies from Table 2. [c]SOC corrections calculated with the CASSCF state interaction approach. Values of 0.00 indicate SOC corrections <10^{-2} kcal/mol.

mass-weighted coordinates was generated utilizing the method of Gonzales and Schlegel[38,39] with variable step size reducing the latter in important regions to a step size of 0.005 amu$^{1/2}$, thus leading in the extreme to 1400 path points (X = Pb). The difference between the energies at the end points and the BSSE-corrected reactant or product energies turned out to be 0.5 kcal/mol or smaller. Typically, it was 0.1 kcal/mol above the reactant (product) energies for X being a second period atom and increased to 0.5 kcal/mol for increasing AN of X.

All avoided crossings between the vibrational eigenstates were resolved using the diabatic mode ordering (DMO) procedure of Konkoli et al.[40] This guarantees a correct representation of curvature coupling and Coriolis coupling coefficients. In all reactions, valley ridge inflection (VRI) points were determined that preceded path bifurcation (BF) points far out in the exit or entrance channel. Physically, the VRI and BF points are caused by either rotation of H_2 out of the symmetry plane of the reaction complex or an in-plane outward (inward) bending of the separating H atom relative to the direction of the newly formed XH bond. For the reactions investigated, these processes have little influence on the reaction mechanism and therefore are not discussed in this work. However, it should be noted that with the occurrence of a VRI point the local mode coefficients A_{ns} may switch their sign, which has to be considered when analyzing the scalar curvature in terms of A_{ns} contributions.

For all 18 reactions, the energy $E(s)$, the reaction path curvature $\kappa(s)$, its decomposition into normal mode curvature coupling coefficients $B_{\mu s}(s)$ and local mode curvature coupling coefficients $A_{ns}(s)$, the reaction path direction $\eta(s)$, and its decomposition into local mode components, the internal coordinate forces $f_n(s)$, the generalized normal-mode frequencies $\omega_\mu^g(s)$ and their conversion into generalized local vibrational mode frequencies $\omega_a^g(s)$, the Coriolis coupling coefficients $B_{\mu\nu}(s)$, and the internal coordinates $q_n(s)$ describing the changes of the reaction complex were calculated along the reaction path.[1,2]

At the minima of the scalar curvature $\kappa(s)$, the geometry and the charge distribution of the reaction complex were analyzed where for the charges MP2 response densities[41] were used, which were analyzed utilizing the natural bond orbital (NBO) approach.[42,43] Also, the NBO charges were determined as functions of the path parameter s.

The URVA and NESC calculations were carried out with the COLOGNE2012 quantum chemical program package.[44] For the CCSD(T) geometry and frequency calculations, the program package CFOUR was employed.[45] The MOLPRO 2010 program package[46] was used for the SOC CASSCF state interaction calculations.

3. RESULTS AND DISCUSSIONS

In Table 1, reaction energies ΔE_R and activation energies ΔE^a calculated at the NESC/SOC/CCSD(T)/cc-pV5Z level of theory are listed. NESC/CCSD(T)/cc-pVTZ geometries are shown in Figures 1 and 2. Also listed in Table 1 are enthalpy values at 298 K ($\Delta H_R(298)$ and $\Delta H^a(298)$) and the corresponding free energy differences $\Delta G_R(298)$ and $\Delta G^a(298)$ where both sets of data have been obtained by calculating vibrational, thermochemical, and entropy corrections with the help of CCSD(T)/cc-pVTZ frequencies. Where possible, experimental enthalpies derived from the heats of formation at 298 K, $\Delta H_f^o(298)$,[47,48] given in Table 2 or taken directly from the literature are also included.[49−53] NESC/SOC/CCSD(T)/cc-pV5Z and experimental bond dissociation enthalpies (BDEs) for the reaction $XH_{n+1} \rightarrow XH_n + H$ are also given in Table 2. Furthermore, Table 2 contains all SOC corrections and imaginary frequencies of the TSs. Since a dual level approach is used in this work, the reaction path energies obtained at the UMP2/6-31G(d,p) level of theory are also included in Table 1, although they provide just a qualitative insight into the energetics of the 18 reactions investigated.

Reaction Phases and Transient Structures. In Figure 3, the curvature diagrams of the 18 reactions are shown. All scalar curvature functions $\kappa(s)$ are analyzed in terms of local mode curvature coupling (LMCC) coefficients $A_{ns}(s)$ so that for each

H—H 0.743 F—H 0.917 Cl—H 1.277 Br—H 1.410 I—H 1.605

O—H 0.971 S—H 1.345 Se—H 1.473 Te—H 1.654
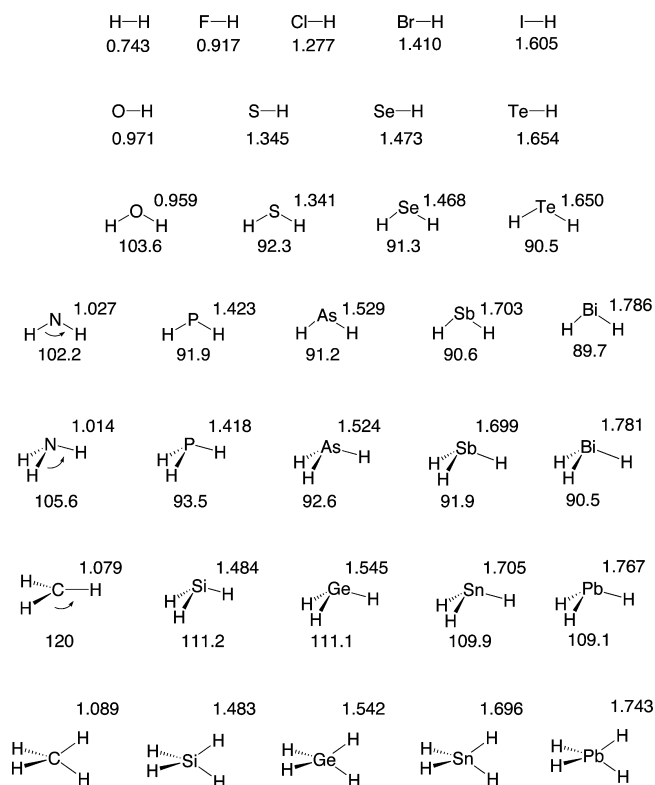
Figure 1. NESC/CCSD(T)/cc-pVTZ geometries of XH_n and XH_{n+1} molecules with X = F, Cl, Br, I, O, S, Se, Te, N, P, As, Sb, Bi, C, Si, Ge, Sn, Pb. Bond lengths in Å, angles in deg.

reaction phase the dominant structural change (reflected by internal coordinate q_n (bond lengths XkYl or bond angles XkYlZm; k, l, m refer to the numbers of the atoms of $XH_n \cdots H_2$) of the reaction complex can be identified. We will discuss here the curvature diagram and the mechanism of the reaction NH_2

+ H_2 (Figures 3c and 4) as a suitable example. This reaction proceeds with a four-phase mechanism, which can be further detailed to a six-phase mechanism considering the broad shoulder between 0.7 and 1.7 s units and the slope region between −2.8 and −2.3 s units as separate phases (s units are amu$^{1/2}$ bohr). The inclusion of additional Mn points thus leading to a six-phase mechanism is justified by the analysis of the internal coordinate functions $q_n(s)$, the reaction path direction in terms of local mode contributions, and the change in the atomic NBO charges along the path (Figure 4), however, especially in the van der Waals regions of entrance and exit channel.[1,6] The same analysis has been applied to all 18 reactions and is the basis for Table 3, where the mechanisms of all 18 reactions are presented by highlighting the relevant reaction phases. It has to be noted that in Figure 3 as well as Table 3, the numbering of the path points Mn corresponds to an ideal mechanism comprising six phases and six Mn points, which for a real reaction system may not all be present. In the following, the six-phase mechanism of the NH_2 + H_2 reaction is discussed.

Phases 1 and 2 (orientation, charge transfer, and polarization; from −2.75 s units to M4; preparation phase from M4 to M2): The NH_2 radical possesses a single, unpaired electron in the $p\pi(N)$ orbital and has a dipole moment of 1.82 D.[54] If the two molecules approach each other in a parallel fashion (angles H2N1H2 and N1H2H5 are 90°, Figure 3c), NH_2 can induce a dipole moment in H_2, thus leading to mutual attraction between the reactants. This parallel approach however excludes a charge transfer involving the $p\pi(N)$ and $\sigma^*(HH)$ orbitals, which would be most effective for an N1H2H5 angle of 180°. Hence, a compromise between these reaction-decisive inter-actions is found at an N1H2H5 angle of 145°. This angle is sufficient for a mutual polarization of NH_2 and H_2 molecules (12 (H2) and −16 me (H5) at −2.75 s units, see Figure 4), and a 4 me charge transfer from the NH_2 radical to the H_2 molecule. At the end of the orientation phase, density
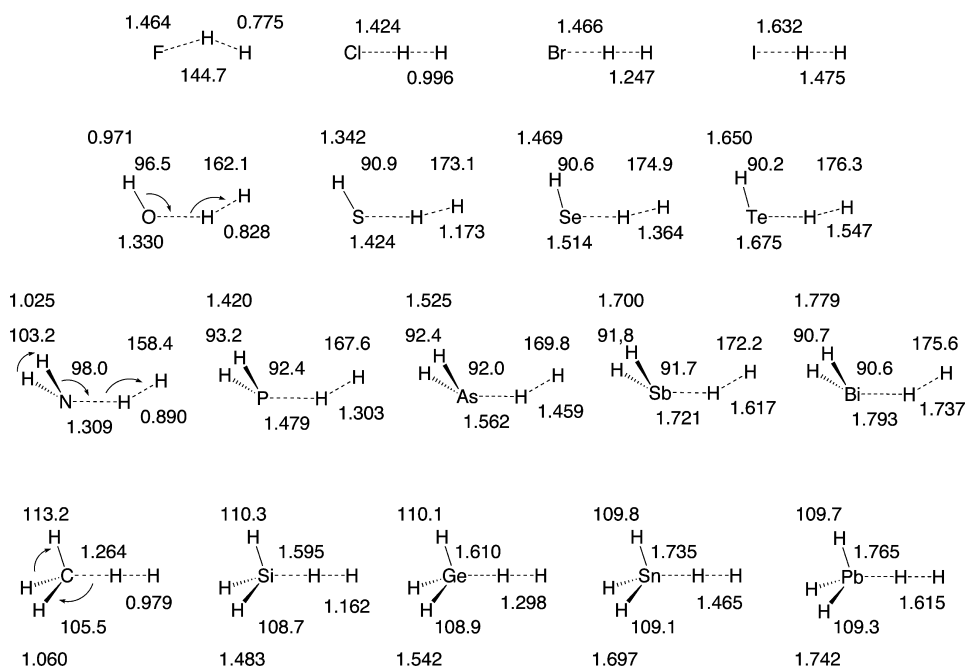
Figure 2. NESC/CCSD(T)/cc-pVTZ geometries of TSs of the reaction XH_n + H_2 → XH_{n+1} with X = F, Cl, Br, I, O, S, Se, Te, N, P, As, Sb, Bi, C, Si, Ge, Sn, Pb. Bond lengths in Å, angles in deg.

Table 2. Spin Orbit Couplings (SOC), Heats of Formation $\Delta H_f^{\circ}(298)$, Bond Dissociation Enthalpies (BDE) at 298 K, and Imaginary Frequencies of the Reaction Complex at the TS[a]

X	SOC[b] XH_n cm^{-1}	$\Delta H_f^{\circ}(298, \text{exptl})$ XH_n kcal/mol	SOC[b] XH_{n+1} cm^{-1}	$\Delta H_f^{\circ}(298, \text{exptl})$ XH_{n+1} kcal/mol	SOC[b] TS cm^{-1}	BDE(298, calcd) XH_{n+1} kcal/mol	BDE(298, exptl) XH_{n+1} kcal/mol	$\omega(\text{TS})^c$ imag cm^{-1}
H	0	52.103 ± 0.07	0	0	0	104.1[e]	104.154 ± 0.02	
F	−101	18.97 ± 0.07	0	−65.32 ± 0.2	0	135.7	136.157 ± 0.003	878 i
Cl	−294	28.992 ± 0.002	−2	−22.06 ± 0.02	−5	102.8	103.099 ± 0.003	1418 i
Br	−1209	26.74 ± 0.03	−43	−8.67 ± 0.04	−48	88.6	87.51 ± 0.05	873 i
I	−2771	25.52 ± 0.01	−273	6.33 ± 0.02	−200	72.0	71.29 ± 0.02	571 i
O	−67	8.93 ± 0.03	0	−57.80 ± 0.01	0	118.3	118.81 ± 0.07	1309 i
S	−174	34.2 ± 0.2	−1	−4.92 ± 0.12	−1	90.8	91.10 ± 0.01	1243 i
Se	−867	34.6 ± 0.5	−33	6.65 ± 0.2	−18	80.5	80.05 ± 0.18	831 i
Te	−2101	37.9 ± 1.2	−234	24.95 ± 0.5	−93	66.6	65.0 ± 0.1	576 i
N	0	44.5 ± 0.2	0	−10.97 ± 0.09	0	107.0	107.57 ± 0.06	1599 i
P	0	33.1 ± 0.6	0	1.3 ± 0.5	0	82.5	83.9 ± 0.5	1003 i
As	−14	40.1 ± 0.3	−8	15.90 ± 0.1	−9	76.1	76.3 ± 0.2	723 i
Sb	−93	51.5 ± 0.6	−61	34.70 ± 0.3	−65	68.3	68.9 ± 0.5	518 i
Bi	−1544	38.1[d]	−994	25.6 ± 1.0	−1033	64.5	na	441i
C	0	35.06 ± 0.1	0	−17.89 ± 0.10	0	104.5	105.0 ± 0.1	1302 i
Si	0	47.9 ± 0.6	0	8.20 ± 0.4	0	91.7	91.7 ± 0.5	1278 i
Ge	−1	53.0 ± 2.0	−1	21.7 ± 2	0	84.6	83.4 ± 2	981 i
Sn	−31	64.2[d]	−10	38.9 ± 2	−5	77.3	na	685 i
Pb	−735	80.9[d]	−191	59.4 ± 2	−75	73.5	na	551 i

[a]Experimental heats of formation from refs 47 and 48. [b]SOC corrections calculated with the CASSCF state interaction approach using a Breit−Pauli operator. Values of 0 indicate SOC corrections <1 cm^{-1}. [c]ω(TS) imag denotes the imaginary frequency at the TS. [d]Calculated enthalpy; this work. [e]After anharmonicity correction.

polarization and charge transfer have led to a lengthening of the HH bond from 0.734 to 0.744 Å.

Phase 3 (HH bond breaking phase; from M2 to M1): From the curvature minimum M2 on, the charge transfer is reversed from −5 (i.e., 5 me are donated to H_2) to +68 me (see Figure 4). After the HH bond has been weakened by charge transfer into its antibonding MO in phases 1 and 2 (thus simplifying the polarization of the electron density distribution of H_2), the actual HH bond breaking is caused by charge withdrawal from the bonding σ(HH) orbital. Curvature peak K1 is dominated by the H2H5 LMCC coefficient (Figure 3c). At the end of this phase, the HH distance is 0.997 Å and the NH distance has been reduced to 1.186 Å. A transient nonlinear 3e−3c complex (N1H2H5 angle of 159°) is formed between NH_2 and H_2.

Phase 4 (NH bond forming phase; from M1 to M5): In this phase, a new NH bond is formed, which is confirmed by the fact that curvature peak K2 is dominated by the N1H2 LMCC coefficient (Figure 3c). The NH bond adopts a length typical of NH_3 (1.012 Å) and much shorter than that for the NH_2 radical (1.024 Å). In this phase, the LMCC coefficient H2H5 takes a negative value, thus indicating a resistance of further separation of these two atoms. It has to be noted in this connection that at the VRI points the LMCCs change their sign.) This resistance is found in phase 3 (as well as phases 1 and 2) with regard to the N1,H2 approach and clarifies that in the range K1 to K2, HH cleavage and NH bond formation take place simultaneously, however with different roles. Up to a central point given by M1, the reaction is first driven by the charge withdrawal from the σ(HH) orbital into the $p\pi$(N) orbital where the NH bond formation via the establishment of a doubly occupied σ(NH) orbital is resisting. At M1, the two roles are switched. Hence, M1 is the center of the bond cleaving and forming processes, which is true for all 18 reactions. This is nicely reflected by the NBO charges of N1

and H2, which possess inflection points M1, i.e., N is at this point halfway from a divalent to a trivalent atom, the spectator bonds N1H3 and N1H4 adjust to the situation in NH_3, and H2 is halfway to becoming an NH_3 hydrogen.

Phase 5 (rehybridization and adjustment of the NH_3 charge distribution; from M5 to M6): The separating H atom becomes positively charged (see Figure 4) and polarizes the charge distribution of NH_3, especially that of the newly formed NH bond. Therefore, the density of the latter NH bond (not to be confused with that of H2) is higher than that of a normal NH bond in NH_3. Consequently, the bond length is further reduced (strengthened) to 1.009 Å (at s = 1.72 s units at the end of the curvature shoulder and the position of M6)

Phase 6 (product finalization phase; from M6 to a BP at the end of the reaction path): In this phase, charge is transferred back from NH_3 to the H atom. The NH_3 molecule relaxes from C_s to local C_{3v} symmetry. All three NH bonds adopt the same bond length of 1.012 Å; i.e., the newly formed NH bond lengthens to 1.012 due to charge reorganization in NH_3. The separating H atom wants to leave the symmetry plane and to move into a position farther removed from the positively charged H atoms bonded to N. Since there are two equivalent possibilities, the path bifurcates. The ridge, which starts at the VRI point shortly after the TS, is only slightly (0.1 kcal/mol) above the two valleys, and therefore the ridge path is still a representative path. Actually, there is another VRI point associated with an in-plane bending motion of the separating H atom.

Similar mechanisms are found for all 18 reactions, however with some important changes (see Table 3). If X is a second period atom such as C, N, or O, the reaction mechanism includes rehybridization and charge redistribution phases, which are not found for X atoms from higher periods. For example, the first curvature enhancement at s = −2.5 units of
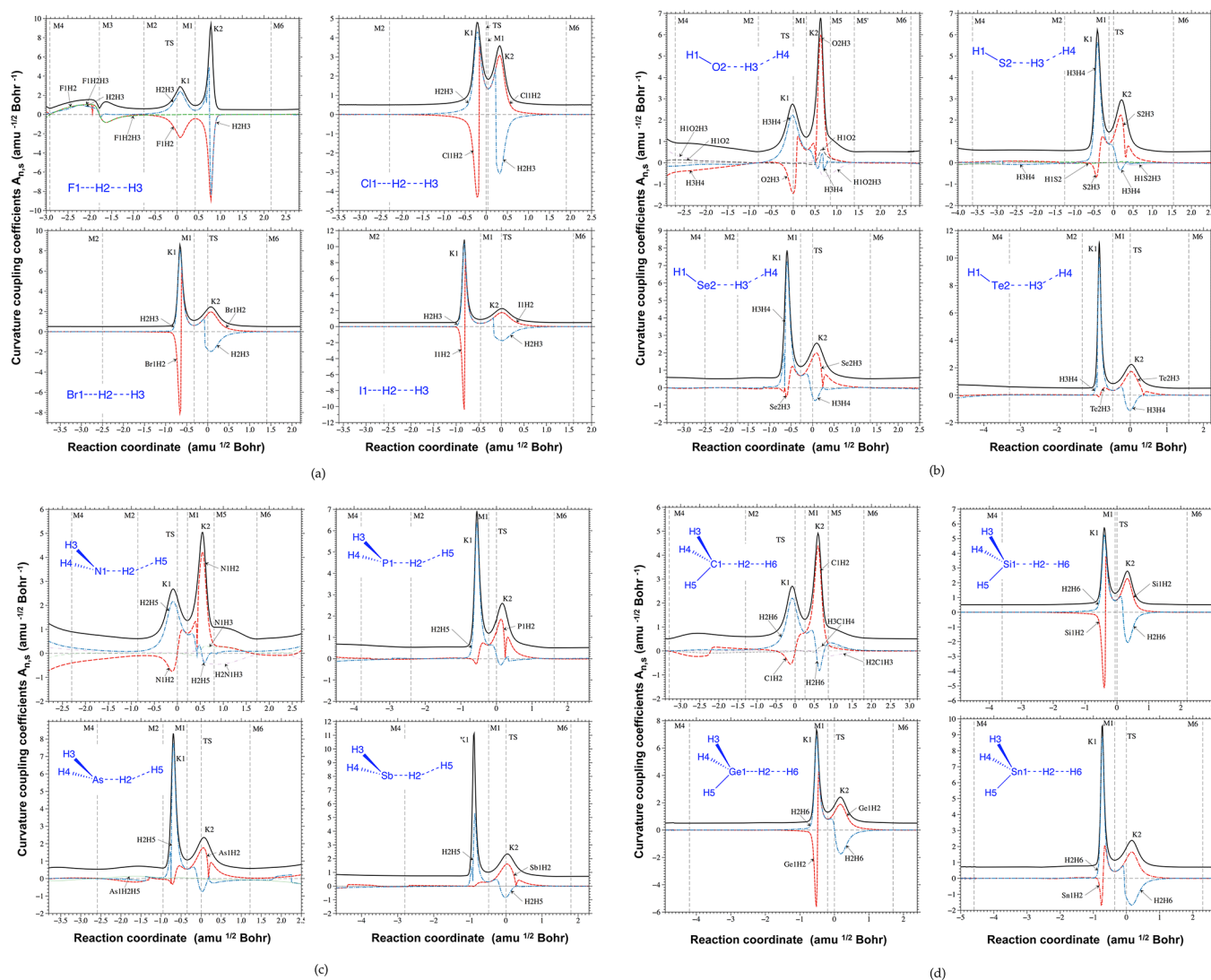
Figure 3. Curvature diagrams of the 18 reactions $XH_n + H_2 \rightarrow XH_{n+1} + H$ representing the change of the scalar curvature $\kappa(s)$ (bold black line) given as a function of the reaction path parameter s. Each curvature function is analyzed in terms of local mode curvature coupling coefficients A_{ns} (dashed lines), which are identified by the symbols $XkYl$ (bond lengths) and $XkYlZm$ (bond angles). The TS at $s = 0$ amu$^{1/2}$ bohr is given by a dashed vertical line. The positions of the curvature minima (or mechanistically relevant curvature points) Mn are also indicated by dashed vertical lines. The region between two neighboring Mn points is a well-defined reaction phase of the reaction mechanism where typical electronic structure changes of the reaction complex take place (compare with Table 3). Mn points are numbered to comply with a general phase pattern established in Table 3. The numbering of the atoms in the reaction complex is given for each reaction. (a) X = F, Cl, Br, I; (b) X = O, S, Se, Te; (c) X = N, P, As, Sb; (d) X = C, Si, Ge, Sn.

the reaction $CH_3 + H_2$ (see Figure 3d) indicates the rehydbridization of the planar CH_3 radical to a pyramidal one. This curvature enhancement is missing for X = Si, Ge, Sn, or Pb because in these cases the XH_n radical is most stable in the pyramidal form, which is a consequence of the reduced possibility of orbital hybridization (due to increased ns−np energy gaps) in these cases. Similarly, the shoulder of curvature peak K2 between M5 and M6 of the $CH_3 + H_2$ reaction relates to the rehybridization accompanying a symmetry change from C_{3v} to T_d symmetry (actually the reaction complex maintains C_{3v} symmetry; however, with increasing separation of the H atom from CH_4, the latter molecule adopts T_d symmetry and sp^3 hybridization at the C atom).

It is interesting to note that for the reverse reaction (attack of an H atom at an X−H bond) this rehybridization step leads first to a shortening of the XH bond being attacked before charge transfer, charge polarization, and finally charge with-

drawal leads to a cleavage of the XH bond. Although this effect is small (reduction of the NH bond length by 0.003 Å in the case of NH_3), it can be reproduced at all levels of theory used in this work. Similar reductions can be found for H_2 if X is strongly electronegative. Hence, rehybridization implies often that the bond to be broken first becomes stronger.

The orientation phase plays an important role for the reactions involving NH_2, OH, and F, however less for its higher homologues, which is a result of the decreasing electronegativity of the atom X and its decreasing polarizing ability. It is interesting that the anisotropy of the electron density distribution at an F(^{2}P) atom (because of the missing electron there is a hole in a spherical charge distribution) leads to a bent rather than linear arrangement with a bending angle of 145° at the TS (Figure 2), again indicating a compromise between charge polarization and charge transfer. At the curvature minimum M3 (Figure 3a, X = F), the direction of the charge

4936

dx.doi.org/10.1021/ct300631s | J. Chem. Theory Comput. 2012, 8, 4931−4943
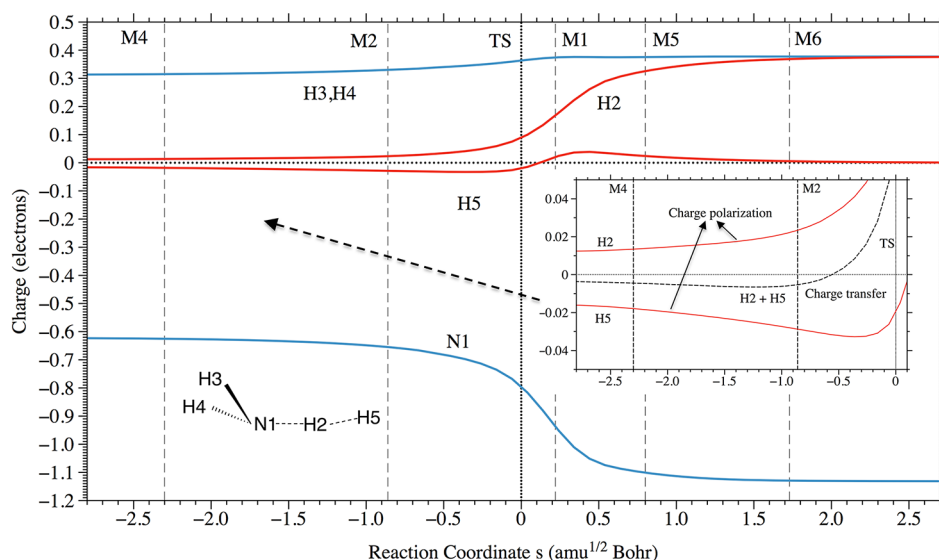
Figure 4. NBO charges of the reaction complex $H_2N\cdots H\cdots H$ given as a function of the reaction parameter s. The inset gives the charge transfer from NH_2 to the $\sigma^*(HH)$ orbital (dashed black line) and the charge polarization of H_2 (red lines, H2 positively charged; H5 negatively charged) in the entrance channel.

Table 3. Mechanistic Analysis; Reaction Phases and Structural Changes of the Reaction Complex[a]

X	phase 1	phase 2	phase 3	phase 4	phase 5	phase 6	mechanism
F	orient+ct	prep	HH cleav	FH form		final	withdrawal from $\sigma(HH)$
Cl		prep	HH cleav	ClH form		final	withdrawal from $\sigma(HH)$
Br		prep	HH cleav	BrH form		final	withdrawal from $\sigma(HH)$
I		prep	HH cleav	IH form		final	donation to $\sigma^*(HH)$
O	orient+ct	prep	HH cleav	OH form	rehy	final	withdrawal from $\sigma(HH)$
S	orient+ct	prep	HH cleav	SH form		final	withdrawal from $\sigma(HH)$
Se	orient+ct	prep	HH cleav	SeH form		final	withdrawal from $\sigma(HH)$
Te	orient+ct	prep	HH cleav	TeH form		final	donation to $\sigma^*(HH)$
N	orient+ct	prep	HH cleav	NH form	rehy	final	withdrawal from $\sigma(HH)$
P	orient+ct	prep	HH cle av	PH form		final	donation to $\sigma^*(HH)$
As	orient+ct	prep	HH cleav	AsH form		final	donation to $\sigma^*(HH)$
Sb		prep	HH cleav	SbH form		final	donation to $\sigma^*(HH)$
Bi		prep	HH cleav	BiH form		final	donation to $\sigma^*(HH)$
C	ct	rehy	HH cleav	CH form	rehy	final	withdrawal from $\sigma(HH)$
Si		prep	HH cleav	SiH form		final	donation to $\sigma^*(HH)$
Ge		prep	HH cleav	GeH form		final	donation to $\sigma^*(HH)$
Sn		prep	HH cleav	SnH form		final	donation to $\sigma^*(HH)$
Pb		prep	HH cleav	PbH form		final	donation to $\sigma^*(HH)$

[a]The following abbreviations have been used: orient, orientation; ct, charge transfer; cleav, cleavage; form, formation; rehy, rehybridization; final, finalization.

transfer is reversed, and F changes from a donor to an acceptor. These details are no longer found for the reactions $X + H_2$ with $X = Cl$, Br, and I because the polarizing power of these atoms is too small, and therefore the reaction complex is linear throughout the reaction.

The detailed analysis of all 18 reactions reveals a number of similarities and differences. There are two different HH cleavage mechanisms, which do depend on the electronegativity of X. For the more electronegative atoms $X = F, O, N, C, Cl, S, Br$, and Se, HH bond cleavage is caused by charge withdrawal. This however is preceded by charge transfer to the $\sigma^*(HH)$ orbital, which facilitates the polarization of the HH bond. For the second group containing the more electropositive atoms $X = I, Te, P, As, Sb, Bi, Si, Ge, Sn$, and Pb, charge is donated from the $p\pi(X)$ orbital of XH_n into the $\sigma^*(HH)$ orbital, in this way facilitating polarization and bond cleavage. According to the

electronegativity of X the charge pattern in the polarized HH is either $+-$ for the first group or $-+$ for the second group, where the first sign is for the vicinal and the second is for the distal H atom.

The distinct curvature minimum between K1 and K2 represents in all cases a nonclassical 3e−3c system $X\cdots H\cdots H$ with interaction distances being 0.2−0.25 Å longer than normal XH or HH bond lengths. A stabilization of such a transient structure to become a real intermediate is possible if X is substituted by strongly electronegative atoms or groups. In this way, an effective 2e−3c nonclassical system is formed. Hence it is justified to associate M1 with a hidden intermediate. The structures of the XHH M1 intermediates in the sense of more or less bending can be discussed in view of a pseudo-Jahn−Teller effect, which is larger for strongly electronegative X,

thereby leading to a low-lying excited state of the same symmetry.

Energetics of the Reaction in Comparison with Other Results. For most of the 18 reactions, especially the strongly endothermic reactions with low barriers for the reverse reaction, experimental activation enthalpies $\Delta H^a(298)$ could not be measured (Table 1). Also, the reaction enthalpies $\Delta H_R(298)$ are not known or known only with large error bars for the heavy elements with atomic numbers AN ≥ 50. In Table 2, we have summarized all known measured heats of formations $\Delta H_f^\circ(298)$ and compare calculated and experimental bond dissociation enthalpies (BDE) for $XH_{n+1} \rightarrow XH_n + H$.[47,18] Calculated SOC corrections for all molecules investigated and the NESC/CCSD(T)/cc-pVTZ imaginary frequencies at the TS are also given in Table 2.

The SOC corrections of Table 2 show the known dependency on the AN in case of a degenerate ground state leading to a first order SOC effect; i.e., the value of the SOC correction increases with the fourth power of AN,[55] which is the case for the halogen atoms and the XH radicals with X being a chalcogen. In all other cases, the second order SOC effect is dominant, which is proportional to the reciprocal of the excitation energies ΔT_e.[56,57] With increasing hydrogenation, the value of ΔT_e increases, thus reducing the SOC correction from XH_2 to XH_3 provided there is a fractional occupation of the p orbitals as in the XH_n radicals. Again, the dependence of the SOC correction on the AN is obvious (see Table 2).

For those systems with reliable $\Delta H_f^\circ(298)$ data, calculated and measured BDE values differ on the average by 0.68 kcal/mol, which provides an excellent basis for the discussion of the energetics of reaction 1. For X = Bi, Sn, and Pb, reliable BDE values are not known. We obtain 64.6 (X = Bi), 77.4 (Sn), and 73.6 kcal/mol (Pb; Table 2). With these BDE values, we have calculated the missing $\Delta H_f^\circ(298)$ data for radicals BiH_2, SnH_3, and PbH_3, which are 38.1, 64.2, and 80.9 kcal/mol, respectively (see Table 2).

The BDE values of Table 2 suggest that the replacement of the HH bond by an XH bond is only energetically favorable for X being a second period element. The process becomes increasingly unfavorable and by this increasingly endothermic ($\Delta H_R(298)$ values up to 40 kcal/mol, Table 1) for increasing AN of X. For the highly endothermic reactions, the values of $\Delta H^a(298)$ are only slightly above those of $\Delta H_R(298)$, suggesting that in the presence of H atoms rapid formation of H_2 and XH_n radicals is the rule although X−H BDEs of the closed shell molecules XH_{n+1} are ≥60 kcal/mol (see Table 2). This means that the XH bonds in these cases can be easily polarized and broken by an attacking H atom, which is confirmed by the curvature diagrams (reflected by low curvature peaks K2, see Figure 3). There is first a small charge transfer from the attacking H atom into the $\sigma^*(XH)$ bond orbital and charge polarization toward the more electronegative H atom (compared to X for large AN). At short-range, the polarization of the XH bond helps to withdraw negative charge from XH and to form the HH bond.

Of the 18 reaction systems investigated, the system F + H_2 is the best studied.[58,61] The experimental $\Delta H_R(298)$ value is −32.2 kcal/mol,[47] and the $\Delta H^a(298)$ value has been estimated to be <1 kcal/mol.[49,50] Our CCSD(T)/cc-pV5Z enthalpies of −31.6 and 0.3 kcal/mol agree excellently with experimental results. Lower level calculations fail to describe the bending angle correctly, which has also been observed by other authors.[58,60,62] Werner and co-workers[61] did very accurate

calculations on the energy barrier. They did not calculate $\Delta H^a(298)$; however, their value of $\Delta E^a = 1.6$ kcal/mol would lead with the vibrational corrections obtained in this work to a $\Delta H^a(298) \approx 0$ kcal/mol. Using the diffusion Monte Carlo method, Lu[63] obtained $\Delta E^a = 1.1$ kcal/mol, which would correspond to a negative $\Delta H^a(298)$ value.

The reaction Cl + H_2 plays an important role in atmospheric chemistry and photochemical air pollution.[64] The system has been frequently used for the development of TS models.[65−67] Classical barrier heights between 7.61 and 7.88 kcal/mol have been reported.[65] We calculate a barrier height of 8.8 kcal/mol and an activation enthalpy of 4.8 kcal/mol at the CCSD(T)/pV5Z level of theory. The corresponding $\Delta H_R(298)$ value is 1.3 kcal/mol in good agreement with the value of 1.1 kcal/mol derived from experimental $\Delta H_f^\circ(298)$ values.[47]

The reaction Br + H_2 has been used as a prototype for a heavy−light−light system in which SOC corrections adopt an important role (3.3 kcal/mol, see Table 1).[68,69] Recently, Xie and co-workers derived a PES based on MRCI calculations including SOC corrections.[69] They report a classical barrier of 19.1 kcal/mol and a ΔE_R of 17.8 kcal/mol. The measured $\Delta H_R(298)$ is 16.7 kcal/mol (see Table 1). Our NESC/CCSD(T) values for $\Delta H_R(298)$ and $\Delta H^a(298)$ are 15.5 and 16.3 kcal/mol, respectively.

Much work has been recently devoted to the investigation of the potential release of volatile iodine from the nuclear fuel cycle to the environment. Radio-iodine is one of the most radiotoxic fission products and is highly reactive.[70,71] Louis and co-workers[72] performed an extensive kinetic modeling study of I-containing reaction systems including the I + H_2 reaction. They report CCSD(T)/aug-pVTZ reaction and activation enthalpies of 27 kcal/mol (based on MP2 and DFT geometries and frequencies including also an empirical SOC correction) and 34.5 kcal/mol (MP2/aug-pVTZ), respectively. The experimental $\Delta H_R(298)$ is 32.9 kcal/mol (see Table 1), which is in perfect agreement with our NESC/SOC/CCSD(T) $\Delta H_R(298)$ value of 32.1 kcal/mol. Hence, the $\Delta H^a(298)$ of 32.2 kcal/mol obtained in this work is probably the most reliable value obtained so far.

The reaction of the OH($^2\Pi$) radical with H_2 is of importance for atmospheric and combustion chemistry as well as for many other parts of chemistry. Because of its importance, it has become one of the most thoroughly computationally investigated four-atom reactions.[73−75] It is also the principal source of water in hydrogen/oxygen flames[74,75] whereas the reverse reaction is an effective source of OH radicals, which play a key role in atmospheric chemistry.[76,77] Several extensive summaries of quantum chemical calculations are given in the literature.[62,78,79] The measured values for $\Delta H_R(298)$ and $\Delta H^a(298)$ are −14.6 and 4 ± 0.5 kcal/mol[51] (see Table 1), which agree well with our CCSD(T)/pV5Z values of −14.2 and 4.6 kcal/mol, respectively.

The SH + H_2 reaction was investigated experimentally and theoretically with an emphasis on reaction dynamics in the latter case.[80−82] The energetics of the reactions with X = O and X = S are different, which is a consequence of the weaker SH bonds. The reaction of H atoms with H_2S shows a strong non-Arrhenius behavior, which was attributed to tunneling effects.[83] The CCSD(T)/pV5Z enthalpy differences are 13.3 (reaction) and 15.5 kcal/mol (activation), respectively, where the first value is in good agreement with the measured value of 13.0 kcal/mol (see Table 1).

There have been no studies of the reactions HSe + H_2 and HTe + H_2. However, TeH_2 was studied as a prototype for heavy hydrides.[84−87] From measured $\Delta H_f^o(298)$ values, $\Delta H_R(298)$ of 24.2 and 39.2 kcal/mol (Table 1) can be derived with uncertainties of 0.5 and 1 kcal/mol, respectively. The CCSD(T)/cc-pV5Z values are 23.7 and 37.5 kcal/mol, respectively, thus confirming the high endothermicity of these reactions. In view of the calculated activation enthalpies (24.4 and 38.2 kcal/mol, Table 1), the reverse reaction with activation enthalpies of 0.7 and 0.5 kcal/mol will take place rapidly if hydrogen selenide or hydrogen telluride (tellurane) are in the presence of H atoms.

The NH_2 + H_2 reaction has been studied both by theory[62,88−90] and by experimentation,[91] where the focus has been more on the energetics and dynamics of the reaction rather than its mechanistic details. It is noteworthy that the reverse reaction NH_3 + H plays an important role in the chemistry of the ammonia pyrolysis at high temperatures. The experimental $\Delta H_R(298)$ and $\Delta H^a(298)$ values are −3.4 and 8.5 ± 0.5 kcal/mol[52] (see Table 1). The corresponding CCSD(T)/cc-pV5Z values are −2.9 and 9.5 kcal/mol in good agreement with experimental results.

The dynamics of the reaction PH_3 + H were previously investigated.[92] The reactions of H atoms with PH_3 and its higher homologue AsH_3 are considered to play a significant role in the mechanism of metal organic chemical vapor deposition (MOCVD) processes used when manufacturing III−V semiconductor materials.[93−95] They are also thought to be involved in forming trace amounts of PH_3 and AsH_3 found in the atmospheres of Jupiter and Saturn.[96] The PH_2 + H_2 reaction is endothermic by 20.3 kcal/mol (see Table 1) in reasonable agreement with a CCSD(T)/cc-pV5Z value of 21.6 kcal/mol. The activation enthalpy is 23.4 kcal/mol, which suggests a $\Delta H^a(298)$ value of 1.8 kcal/mol for the reverse reaction; i.e., H atoms rapidly split a PH bond thus generating PH_2 radicals.

We calculate an even smaller $\Delta H^a(298)$ value of 0.6 kcal/mol for the reaction AsH_3 + H due to the fact that the enthalpy differences for the forward reaction are 28.0 (exptl.: 27.9 kcal/mol, Table 1) and $\Delta H^a(298)$ = 28.6 kcal/mol, respectively. The corresponding values for the reaction SbH_3 + H are 35.8 and 35.9 kcal/mol, respectively, leading to an activation enthalpy of 0.1 kcal/mol for the reverse reaction. Neither forward nor reverse reaction have been investigated for X = Sb, although SbH_3 has been studied.[97−99]

An experimental value for the reaction BiH_2 + H_2 cannot be derived because the heat of formation of the BiH_2 radical is not known (however BiH_3 was experimentally investigated[76]). We derive from the calculated $\Delta H_R(298)$ = 39.6 kcal/mol (see, Table 1) and the measured $\Delta H_f^o(298, BH_3)$ = 25.6 kcal/mol a $\Delta H_f^o(298, BH_2)$ value of 38.1 kcal/mol for the radical. The calculated $\Delta H^a(298)$ value is 38.9 kcal/mol (see Table 1), which is 0.7 kcal/mol lower than $\Delta H_R(298)$ and suggests that BiH_3 cannot be formed in this way.

The reaction between the planar CH_3 radical and the H_2 molecule has been extensively studied by experimentation and theory. Recent studies[100−103] focus predominantly on the reaction dynamics. An early rather accurate account on the energetics of the reaction was given by Kraka and co-workers.[62] The mechanism of the CH_3 + H_2 reaction was discussed by Konkoli et al.[1] The reaction is almost thermoneutral, as indicated by the calculated $\Delta H_R(298)$ of −0.4 kcal/mol, which is in good agreement with the corresponding experimental value of −0.85 kcal/mol (Table 1). The same holds for

experimental and calculated $\Delta H^a(298)$ values: 10.9 ± 0.5[53] vs 10.1 kcal/mol (Table 1).

The basic difference between the reactions CH_3 + H_2 and SiH_3 + H_2 is that the reacting radical is planar in the former and pyramidal in the latter case, which leads to a simpler mechanism for X = Si because the pyramidalization step is no longer needed. The reaction SiH_3 + H_2 and related hydrosilane reactions have been studied theoretically[104,105] and experimentally.[106] A recent review discusses the importance of hydrosilanes in transition metal chemistry.[107] The reaction SiH_3 + H_2 is (as all reactions with X being a third, fourth, or fifth period atom) endothermic: $\Delta H_R(298)$ = 12.4 kcal/mol are obtained from both experimental heats of formations and the CCSD(T)/cc-pV5Z calculations of this work. The calculated $\Delta H^a(298)$ value is 15.9 kcal/mol, again indicating a lowering of the reverse barrier for increasing atomic number of X.

The reaction GeH_3 + H_2 is significantly more endothermic ($\Delta H_R(298)$ = 20.8 (exptl.) vs 19.5 kcal/mol, see Table 1) than those of the lower homologues. The calculated activation enthalpy is 21.2 kcal/mol, which suggests that the reverse reaction has a small $\Delta H^a(298)$ value of 1.7 kcal/mol. There are kinetic studies of the reaction GeH_4 + H which agree with the results of this work by suggesting an almost spontaneous reaction.[108,109] The increase of the endothermicity of the reaction XH_n + H_2 for group IV elements X continues for Sn (NESC/CCSD(T): 26.8 kcal/mol, Table 1) and Pb (CCSD-(T): 30.6 kcal/mol, Table 1). The calculated $\Delta H^a(298)$ values are 27.7 (X = Sn) and 30.4 kcal/mol (X = Pb) where for Pb a similar situation as for Bi results. Recent studies focusing on SnH_4 and other stannanes[110,111] as well as PbH_4 suggest that these molecules are stable in line with the calculated BDE given in Table 2.[111,112] However, H atoms will lead to rapid decomposition.

Relationship between Curvature and Activation Energies. Bond breaking depends on a few, closely connected electronic factors: (i) the polarizability of the bond in question, (ii) the polarizing ability of the attacking agent, and (iii) the charge withdrawal or transfer ability of the latter. For example in the reaction F(^{2}P) + H_2, the polarizing ability of F is large because of its large electronegativity, which leads to a high, tightly bonded electron density in the valence shell, which upon approaching the H_2 molecule polarizes the bond electron density smoothly and continuously until the HH bond breaks (BDE 104.2, see Table 2). The corresponding changes in the curvature lead to a small and broad curvature peak (see, Figure 3a).

A H atom, which approaches an FH molecule (from its H side), has a small polarizing ability, and therefore it has to come close to the H atom of the polar FH bond (BDE 136.2, see Table 2) before it is able to polarize and then break the bond. Once this distance has been reached, the breaking of the FH bond proceeds rapidly and all of a sudden is reflected by a large and narrow curvature peak (see, Figure 3a). Hence, the height of the curvature peaks reveals which bond is easier to break in a given reaction: the HH bond by F (small, broad peak) or the FH bond by H (large, narrow peak). The ease of breaking a bond is of course also reflected by the activation energies of a reaction: For the forward reaction F(^{2}P) + H_2, the activation energy is just 2 kcal/mol; however for the reverse reaction FH + H(^{2}S) it is 33 kcal/mol (Table 1).

It turns out that the heights of the curvature peaks reflect the ratios of the activation energies ΔE^a of the forward and reverse reactions. This is shown in Figure 5 where for the 18 reactions
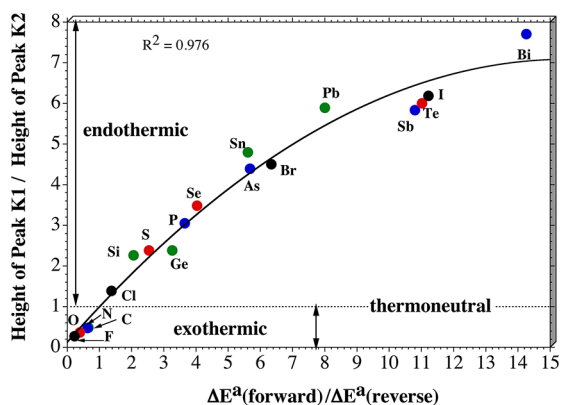
Figure 5. Relationship between the ratio h given by the height of the curvature peaks K1 and K2 and the ratio ρ given by the calculated activation energies ΔE^a of the forward and reverse reactions. An h value smaller than 1 indicates an exothermic, a value larger than 1 an endothermic, and an h value equal to 1 a thermoneutral reaction. The central atom X is given for each $XH_n + H_2 \rightarrow XH_{n+1} + H$ reaction.

investigated the ratios of the heights of curvature peaks K1 and K2 ($h = H1/H2$) is compared with the ratio $\rho = \Delta E^a(\text{forward})/\Delta E^a(\text{reverse})$. The R^2 value for a linear relationship between h and ρ is 0.934, whereas for a quadratic, $R^2 = 0.976$ results. This confirms that the ratio h reflects the energetics of the reaction where with increasing endothermicity of the reaction the height of the large peak K1 increases slower than given by a linear relationship.

For X = Cl, forward and reverse reactions have about the same activation energy, with the reverse reaction being slightly favored; i.e., the forward reaction is endothermic. The Cl atom can no longer as easily polarize the HH bond, and therefore its polarizing power can only develop in a closer approach, which leads to somewhat faster HH bond rupture and a somewhat higher curvature peak K1 (see, Figure 3a). This is even more pronounced for Br and I in line with increasing activation energies for the forward reaction.

Hammond–Leffler Postulate. The Hammond postulate or, better, Hammond–Leffler postulate[10,11] states that TSs of exothermic reactions are reactant-like (early), whereas TSs of endothermic reactions are product-like (late).[113] Various attempts have been made to verify the validity of this hypothesis and to extend it to reactions occurring on catalytic surfaces.[113] However, this implies that a reference point is defined along the reaction path according to which the TS can be considered as being early or late. Apart from the fact that the original postulate was formulated utilizing the free energy rather than the energy itself,[10,11] the energetics of a reaction as given by the relative energies of the stationary points of a reaction do not provide such a reference point. Therefore, a manifold of different approaches based on scaled geometrical parameters, softness and hardness,[114,115] orbital values, electron densities, etc. have been proposed, which either directly or indirectly involve a constructed reference point.[113] Here, we will present a reference point that is directly derived from the reaction mechanism.

In reaction 1, the HH bond is broken and a new XH bond is formed. As discussed above, we can identify by the positions of the curvature peaks K1 and K2 exactly the path range Δs where this event takes place. The curvature minimum M1 between peaks K1 and K2 defines a central point at which the HH bond is halfway broken and the new XH bond halfway formed so that

a transient nonclassical 3e–3c XHH system results (see also Figure 4). By determining the difference $\Delta s(\text{TS})$ between the position of M1 and the TS at $s = 0$ amu$^{1/2}$ bohr and comparing its values with the reaction energy ΔE_R, the quadratic relationship shown in Figure 6 is obtained with an R^2 value of 0.988.
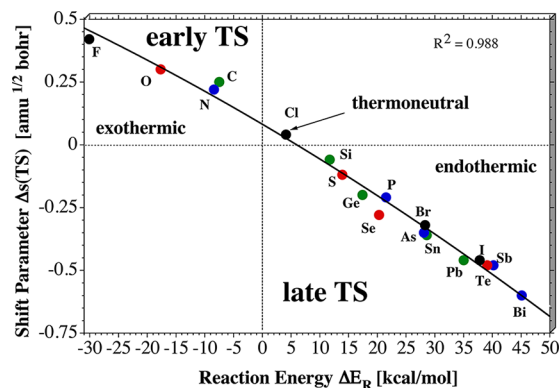
Figure 6. Comparison of the shift parameter $\Delta s(\text{TS})$, which determines the shift of the TS relative to the center of the chemical processes of bond breaking or bond formation, with the reaction energy ΔE_R. A negative $\Delta s(\text{TS})$ value indicates a late TS and a positive $\Delta s(\text{TS})$ value, an early TS. The central atom X is given for each $XH_n + H_2 \rightarrow XH_{n+1} + H$ reaction.

Early TSs as found for exothermic reactions possess a positive $\Delta s(\text{TS})$, which means that the TS is located before M1 in the entrance channel, whereas a negative value of $\Delta s(\text{TS})$ indicates a late TS typical of an endothermic reaction (TS occurs after the position of M1 in the exit channel). The earliness of a TS increases with the exothermicity of the reaction, as can be seen for the reactions with X = N, O, or F (see Figure 6). Similarly, the lateness increases with the endothermicity of the reaction as revealed in the series X = S, Se, Te or X = P, As, Sb, Bi or X = Ge, Sn, Pb.

Although there is some scattering of the data points, which could result from inaccuracies in the UMP2 calculations (they have been used for the path calculations), we conclude that the Hammond–Leffler postulate is fulfilled in a quantitative way for the 18 reactions investigated in this work. The investigation of 20 1,3-dipolar cycloaddition reactions to be published elsewhere is in line with the results of this work. Hence, we conclude that the Hammond–Leffler postulate[10,11] can be verified in general using the curvature of the reaction path.

4. CONCLUSIONS

Accurate reaction and activation energies, enthalpies, and free energies have been obtained for 18 reactions of the type $XH_n + H_2 \rightarrow XH_{n+1} + H$ with X = F, Cl, Br, I, O, S, Se, Te, N, P, As, Sb, Bi, C, Si, Ge, Sn, and Pb using CCSD(T)/cc-pV5Z and NESC/SOC/CCSD(T)/cc-pV5Z. Reaction enthalpies differ from experimental values on the average by 0.68 kcal/mol in those cases where reliable experimental values are known, whereas the calculated activation enthalpies are probably more accurate than the measured values due to the fact that exact experimental values are difficult to obtain in these cases. Based on these results, reliable BDE values of the X–H bond in XH_{n+1} and heats of formation $\Delta H_f^\circ(298)$ of radicals BiH_2, SnH_3, and PbH_3 have been determined.

The importance of SOC corrections has been demonstrated, which determines the trends in calculated reaction and activation energies, especially for systems containing X atoms with high ANs. A first order SOC effect increasing with the fourth power of AN is found for X, being a halogen or chalcogen, whereas second order effects dominate the radicals XH_n with $n = 2, 3$.

Although the 18 reactions are of the same type, their mechanism shows significant differences.

1. For X being a second period element, rehybridization phases can be identified, in which the reaction complex reorganizes its charge distribution. These steps make the mechanism different from that for the systems with an X atom from the higher periods. The reaction mechanism for X being a third, fourth, or fifth period atom is simplified as a direct consequence of the lack of hybridization.

2. For X = F, O, S, Se, Te, N, P, and As, the relative orientation of the reactants accompanied by charge polarization and the induction of a dipole moment, which is facilitated by charge transfer from XH_2 to H_2, precedes the actual weakening of the HH bond. Due to a compromise between electrostatic attraction and charge transfer, XHH bending angles smaller than 170° are found. The anisotropy of the charge distribution of the $F(^2P)$ atom leads even to a bending angle of 145°.

3. Due to rehybridization, an XH bond being attacked becomes first stronger before it is broken.

4. For the more electronegative atoms X, the HH bond is cleaved by charge withdrawal, where for the more electropositive atoms X, the HH bond is cleaved by charge donation and population of the antibonding HH orbital.

5. A nonclassical transient structure of the reaction complex with 3e−3c bonding can be identified at the center of the chemical processes (given by the position of curvature minimum M1), which can be addressed as *hidden reaction intermediate*.

6. For all reactions, bond cleavage and bond formation occur simultaneously. However, in the cleavage phase, HH bond weakening dominates, whereas in the XH bond formation phase the building of a new bond dominates. M1 is the center of the two chemical processes.

The curvature pattern of bond cleavage and bond formation quantitatively reflects the ratio of the activation energies of forward and backward reactions. A small (large) curvature peak for HH bond cleavage and a large (small) curvature peak for XH bond formation indicates an exothermic (endothermic) reaction. The magnitude of the curvature peak is directly related to the polarizability of the bond to be broken and the polarizing ability of the attacking reactant.

The Hammond−Leffler postulate can be quantitatively verified for the 18 reactions investigated with the help of the curvature pattern. The TS is shifted relative to the mechanistic center M1 into the entrance (exit) channel for an exothermic (endothermic) reaction.

For third, fourth, and fifth period elements X, closed shell molecules XH_{n+1} are not stable in the presence of H atoms. XH bond polarization and charge withdrawal requires a low activation energy. Therefore, the system XH_{n+1} + H can only be investigated in the matrix provided at low temperatures (if

generated for example by a photochemical process). At 3 K, activation energies $\Delta E^a(3)$ are 4.7, 1.8, and 1.2 kcal/mol for X = Cl, Br, and I; 3.4, 1.6, and 1.7 kcal/mol for X = S, Se, and Te; 2.6, 1.4, 0.9, and 0.1 kcal/mol for X = P, As, Sb, and Bi; and 4.4, 2.7, 1.6, and 0.5 kcal/mol for X = Si, Ge, Sn, and Pb.

As in previous investigations, the reaction path curvature bears a wealth of mechanistic information, especially if its analysis is combined with the analysis of path direction, generalized vibrational frequencies, charge distribution, and internal coordinates of the reaction complex along the reaction path. We note that the analysis of the reaction path curvature has to be distinguished from the analysis of the one-dimensional energy profile $E(s)$ in terms of its first and second derivative with regard to s (reaction force and reaction force constant) as advocated by Toro-Labbe et al.[116,117] The energy is a cumulative property, and therefore its maximum (TS) and derivatives can only provide information about overall changes of the reaction complex without any details on bond changes, rehybridization, etc. The path curvature is calculated in $3N − (L + 1)$-dimensional space, and its magnitude and direction are analyzed in terms of $3N − (L + 1)$ local vibrational modes, which unravel the changes of the reaction complex in detail.

■ ASSOCIATED CONTENT

ⓢ Supporting Information

This contains calculated geometries and energies for the stationary points of the 18 reactions investigated at the MP2/6-31G(d,p), CCSD(T)/cc-pVTZ, CCSD(T)/cc-pV5Z, and NESC/CCSD(T) levels of theory. This information is available free of charge via the Internet at http://pubs.acs.org.

■ AUTHOR INFORMATION

Corresponding Author

*E-mail: dcremer.at.smu.edu.

Notes

The authors declare no competing financial interest.

■ ACKNOWLEDGMENTS

■ REFERENCES

(1) Konkoli, Z.; Cremer, D.; Kraka, E. *J. Phys. Chem. A* **1997**, *101*, 1742.

(2) Kraka, E. In *Encyclopedia of Computational Chemistry*; Schleyer, P., Allinger, N., Clark, T., Gasteiger, J., Kollman, P., Schaefer, H., III, Schreiner, P., Eds.; Wiley: Chichester, U. K.,1998; Vol. 4; p 2437.

(3) Kraka, E. In *Wiley Interdisciplinary Reviews: Computational Molecular Science*; Allen, W., Schreiner, P. R., Eds.; Wiley: New York, 2011; pp 531−556.

(4) Kraka, E.; Cremer, D. *Acc. Chem. Res.* **2010**, *43*, 591−601.

(5) Cremer, D.; Kraka, E. *Curr. Org. Chem.* **2010**, *14*, 1524−1560.

(6) Kraka, E.; Joo, H.; Cremer, D. *Mol. Phys.* **2010**, *19−20*, 2667.

(7) Kraka, E.; Wu, A.; Cremer, D. *J. Phys. Chem. A* **2003**, *107*, 9008.

(8) Kraka, E.; Cremer, D. *J. Phys. Org. Chem.* **2002**, *15*, 431.

(9) Cremer, D.; Wu, A.; Kraka, E. *Phys. Chem. Chem. Phys.* **2001**, *3*, 674.

(10) Leffler, J. *Science* **1953**, *117*, 340.

(11) Hammond, G. *J. Am. Chem. Soc.* **1955**, *77*, 334.

(12) Raghavachari, K.; Trucks, G. W.; Pople, J. A.; Head-Gordon, M. *Chem. Phys. Lett.* **1989**, *257*, 479−483.

(13) Crawford, T. D.; Schaefer, H. E *Rev. Comput. Chem* **2000**, *14*, 33−136.

(14) Dunning, T., Jr. *J. Chem. Phys.* **1989**, *90*, 1007−1023.

(15) Woon, D.; Dunning, T., Jr. *J. Chem. Phys.* **1993**, *98*, 1358−1371.

(16) Wilson, A.; Woon, D.; Peterson, K.; Dunning, T., Jr. *J. Chem. Phys.* **1999**, *110*, 7667−7676.

(17) Metz, B.; Stoll, H.; Dolg, M. *J. Chem. Phys.* **2000**, *113*, 2563.

(18) Peterson, K.; Figgen, D.; Goll, E.; Stoll, H.; Dolg, M. *J. Chem. Phys.* **2003**, *119*, 11113.

(19) Peterson, K.; Shepler, B.; Figgen, D.; Stoll, H. *J. Phys. Chem. A* **2006**, *110*, 13877.

(20) Peterson, K. *J. Chem. Phys.* **2003**, *119*, 11099.

(21) Berning, A.; Schweizer, M.; Werner, H.; Knowles, P.; Palmieri, P. *Mol. Phys.* **2000**, *98*, 1823.

(22) Roos, B.; Lindh, R.; Malmqvist, P.-A.; Veryazov, V.; Widmark, P.-O. *J. Phys. Chem. A* **2004**, *205*, 2851.

(23) EMSL Basis Set Exchange. https://bse.pnl.gov/bse/portal (assessed June 1, 2012).

(24) Siegbahn, P.; Heiberg, A.; Roos, B.; Levy, B. *Phys. Scr.* **1980**, *21*, 323−327.

(25) Roos, B.; Taylor, P.; Siegbahn, P. *Chem. Phys.* **1980**, *48*, 157−173.

(26) Dyall, K. G. *J. Chem. Phys.* **1997**, *106*, 9618.

(27) Zou, W.; Filatov, M; Cremer, D. *Theor. Chem. Acc.* **2011**, *130*, 633−644.

(28) Zou, W.; Filatov, M; Cremer, D. *J. Chem. Phys.* **2011**, *134*, 244117.

(29) Zou, W.; Filatov, M; Cremer, D. *J. Chem. Theory Comput.* **2012**, *8*, 2617−2629.

(30) Noro, T.; Sekiya, M.; Koga, T. *Theor. Chem. Acc.* **2012**, *131*, 1124.

(31) Noro, T.; Sekiya, M.; Osanai, Y; Miyoshi, E.; Koga, T. *J. Chem. Phys.* **2003**, *119*, 5142.

(32) Miller, W.; Handy, N; Adams, J. *J. Chem. Phys.* **1980**, *72*, 99−112.

(33) Konkoli, Z.; Cremer, D. *Int. J. Quantum Chem.* **1998**, *67*, 1−11.

(34) Konkoli, Z.; Cremer, D. *Int. J. Quantum Chem.* **1998**, *67*, 29−41.

(35) Cremer, D. In *Encyclopedia of Computational Chemistry*; Schleyer, P. v. R., Allinger, N. L., Clark, T., Gasteiger, J., Kollman, P. A., Schaefer, H. E, Schreiner, P. R., Eds.; Wiley: Chichester, U.K., 1998; Vol. 3, p 1706.

(36) Cremer, D. In *Wiley Interdisciplinary: Computational Molecular Science*; Schreiner, P. R., Allen, W., Eds.; Wiley: New York, 2011; Vol. *1*, pp 509−530.

(37) Hariharan, P.; Pople, J. *Theor. Chim. Acta* **1973**, *28*, 213.

(38) Gonzalez, C; Schlegel, H. *J. Chem. Phys.* **1990**, *94*, 523−5527.

(39) Gonzalez, C; Schlegel, H. *J. Chem. Phys.* **1990**, *95*, 5853.

(40) Konkoli, Z.; Cremer, D.; Kraka, E. *J. Comput. Chem.* **1997**, *18*, 1282.

(41) Kraka, E.; Gauss, J.; Cremer, D. *J. Mol. Struct.: THEOCHEM* **1991**, *234*, 95.

(42) Reed, A.; Curtiss, L.; Weinhold, R. *Chem. Rev.* **1988**, *88*, 899−926.

(43) Weinhold, R; Landis, C. R. *Valency and Bonding: A Natural Bond Orbital Donor-Acceptor Perspective*; Cambridge U. Press: New York, 2003.

(44) Kraka, E.; Filatov, M.; Zou, W.; Grafenstein, J.; Izotov, D.; Gauss, J.; He, Y; Wu, A.;Polo, V.; Olsson, L.; Konkoli, Z.; He, Z.; Cremer, D. *COLOGNE12*; 2012; see http://smu.edu/catco/ (assessed June 2012).

(45) Stanton, J. R; Gauss, J.; Harding, M. E.; Szalay, P. G.; et al. CFOUR, a quantum chemical program package. See http://www.cfour.de (accessed June 1, 2012).

(46) Werner, H. J.; Knowles, P. J.; Kniza, G.; Manby, R R.; Schütz, M.; et al. MOLPRO, version 2010.1, a package of ab initio programs. See http://www.molpro.net (assessed June 1, 2012).

(47) Luo, Y.-R. *Comprehensive Handbook of Chemical Bond Energies*; Taylor and Francis Group: New York, 2007.

(48) Johnson, R., III. NIST Computational Chemistry Comparison and Benchmark Database, NIST Standard Reference Database Number 101, Release 15b. http://cccbdb.nist.gov/ (accessed October 2012).

(49) Wiirtzberg, E.; Houston, P. J. *J. Chem. Phys.* **1980**, *72*, 4811.

(50) Heidner, R., III; Bott, J.; Gardner, C; Melzer, J. *J. Chem. Phys.* **1980**, *72*, 4815.

(51) Tully, R; Ravishankara, A. *J. Chem. Phys.* **1980**, *84*, 3126.

(52) Demissy, M.; Lesclaux, R. *J. Am. Chem. Soc.* **1980**, *102*, 2897.

(53) Kerr, J. A.; Parsonage, M. J. *Evaluated Kinetic Data on Gas Phase Hydrogen Transfer Reactions of Methyl Radicals*; Butterworths: London, 1976.

(54) Brown, J.; Chalkley, S.; Wayne, R *Mol. Phys.* **1979**, *38*, 1521−1537.

(55) Sarma, D.; Rao, C. *J. Electron Spectrosc. Relat. Phenom.* **1980**, *20*, 25−45.

(56) Okabayashi, T.; Kawajiri, H.; Umeyama, M.; Ide, C. *J. Chem. Phys.* **2008**, *129*, 124301−1−24301−8.

(57) Koseki, S.; Shimakura, N.; Fujimura, Y; Asada, T.; Kono, H. *J. Chem. Phys.* **2009**, *131*, 004122.1−7.

(58) Aldegunde, J.; Jambrina, P.; de Miranda, M. P.; Rabanos, V.; Aoiz, R *Phys. Chem. Chem. Phys.* **2011**, *13*, 8345−8358.

(59) Ping, W. *J. Theory Comput. Chem.* **2011**, *10*, 111−119.

(60) Lique, R; Li, G.; Werner, H.; Alexander, M. *J. Chem. Phys.* **2011**, *134*, 231101.

(61) Werner, H.-J.; Kallay, M.; Gauss, J. *J. Phys. Chem.* **2008**, *128*, 034305.

(62) Kraka, E.; Gauss, J.; Cremer, D. *J. Chem. Phys.* **1993**, *99*, 5306−5315.

(63) Lu, S.-I. *J. Phys. Chem.* **2005**, *122*, 194323−1−194323−8.

(64) Karamchandani, P.; Zhang, Y.; Chen, S.-Y; Balmori-Bronson, R. *Atmos. Pollut. Res.* **2012**, *3*, 1−14.

(65) Ju, L.; Han, K.; Zhang, J. *J. Comput. Chem.* **2009**, *30*, 305−316.

(66) Xie, T.-T.; Shi, A.-M. *Chin. J. Chem. Phys.* **2007**, *20*, 12.

(67) Humelnicu, I.; Constantinescu, M.; Voicu, I.; Ghirvu, C. *Rev. Roum. Chim.* **2002**, *47*, 817−823.

(68) Zhang, W.; Cong, S.; Zhang, C; Xu, X.; Chen, M. *J. Phys. Chem. A* **2009**, *113*, 4192−4197.

(69) Xie, C; Jiang, B.; Xie, D. *J. Chem. Phys.* **2011**, *113*, 184303.

(70) Koch, L.; Glatz, J.-R; Konings, R. J. M.; Magill, J. *ITU Ann. Rep.* **1999**, *114*, 34−9.

(71) Schlegel, M. L.; Reiller, P.; Mercier-Bion, R; Barre, N.; Moulin, V. *Geochim. Cosmochim. Acta* **2006**, *70*, 5536−5551.

(72) Canneaux, S.; Xerri, B.; Louis, R; Cantrel, L. *J. Phys. Chem. A* **2010**, *114*, 9270−9288.

(73) Nguyen, T.; Stanton, J.; Barker, J. *J. Phys. Chem. A* **2011**, *115*, 5118−5126.

(74) Cavaliere, D. E.; de Joannon, M. *Combust. Sci. Technol.* **2010**, *182*, 692−701.

(75) Castillo, J. R *ChemPhysChem* **2010**, *3*, 320−332.

(76) Seinfeld, J.; Pandis, S. *Atmospheric Chemistry and Physics: From Air Pollution to Climate Change*; Wiley: New York, 2006.

(77) Montzka, S.; Krol, M.; Dlugokencky, R; Hall, B.; Jockel, P.; Lelieveld, J. *Science* **2011**, *331*, 6013.

(78) Althorpe, S.; Clary, D. *Annu. Rev. Phys. Chem.* **2003**, *54*, 493.

(79) Ju, L. P.; Han, K. K.; Zhang, J. *J. Comput. Chem.* **2009**, *30*, 305−316.

(80) Berteloite, C; Lara, M.; Bergeat, A.; LePicard, S.; Dayou, R; Hickson, K.; Canosa, A.; Naulin, C; Launay, J.; Sims, I.; Costes, M. *Phys. Rev. Lett.* **2010**, *105*, 203201.

(81) Gargurevich, I. *Ind. Eng. Chem. Res.* **2005**, *44*, 7706−7729.

(82) Hankel, M.; Smith, S.; Varandas, A. *Phys. Chem. Chem. Phys.* **2011**, *13*, 13645−13655.

(83) Yoshimura, M.; Koshi, M.; Matsui, H.; Kamiya, K.; Umeyama, H. *Chem. Phys. Lett.* **1992**, *189*, 199.

(84) Pernpointner, M. *Chem. Phys.* **2006**, *329*, 256−265.

(85) Underwood, J.; Chastaing, D.; Lee, S.; Wittig, C. *J. Chem. Phys.* **2005**, *123*, 084312.

(86) Alekseyeva, A.; Liebermann, H. P. *J. Chem. Phys.* **2004**, *121*, 9389.

(87) Gumez, P.; Jensen, P. *J. Mol. Spectrosc.* **1997**, *185*, 282−289.

(88) Espinosa-Garcia, J.; Corchado, J. *J. Phys. Chem. A* **2010**, *114*, 6194−6200.

(89) Corchado, J.; Espinosa-Garcia, M.; Yang, J. *J. Chem. Phys.* **2011**, *135*, 014303.

(90) Zhang, X.; Cui, Q.; Zhang, J. *J. Chem. Phys.* **2007**, *126*, 234304.

(91) Friedrichs, H.; Wagner, H. *Z. Phys. Chem.* **2000**, *214*, 1151−1160.

(92) Yu, X.; Li, S.-M.; Liu, J.-Y; Xu, Z.-E; Li, Z.-S.; Sun, C.-C. *J. Phys. Chem. A* **1999**, *103*, 6402−6405.

(93) Yu, X.; Li, S.-M.; Liu, J.-Y; Xu, Z.-E; Li, Z.-S.; Sun, C.-C. *Chem. Phys. Lett.* **2000**, *320*, 123−128.

(94) Smith-Freeman, L.; Schroeder, P.; Wittig, C. *J. Phys. Chem. A* **2009**, *113*, 2158−2164.

(95) Arthur, N.; Cooper, I. *J. Chem. Soc, Faraday Trans.* **1997**, *93*, 521−524.

(96) Morton, R.; Kaiser, R. *Science* **2003**, *51*, 365−373.

(97) Ilander, A.; Vaisanen, A. *Ann. Chim. Acta* **2011**, *689*, 178−183.

(98) Reyes, M.; Cervera, M.; de la Guardia, M. *J. Braz. Chem. Soc.* **2011**, *22*, 197−203.

(99) Wang, X.; Souter, P.; Andrews, L. *J. Phys. Chem. A* **2003**, *107*, 4244−4249.

(100) Schiffel, G.; Manthe, U. *J. Chem. Phys.* **2010**, *132*, 084103.

(101) Zhou, Y; Fu, B.; Wang, C; Collings, M.; Zhang, D. *J. Chem. Phys.* **2011**, *134*, 064323-1−064323-8.

(102) Nyman, G.; van Harrevelt, R.; Manthe, U. *J. Phys. Chem. A* **2007**, *111*, 10331−10337.

(103) Camden, J.; Bechtel, H.; Ankeny Brown, D.; Zare, R. *J. Chem. Phys.* **2005**, *123*, 0134301-1−−13401-9.

(104) Cao, J.; Zhang, Z.; Zhang, C; Bian, W.; Guo, Y. *J. Chem. Phys.* **2011**, *134*, 024315.

(105) Raghunath, P.; Lin, M. *J. Phys. Chem. A* **2010**, *114*, 13353−13361.

(106) Shuman, N.; Spencer, A.; Baer, T. *J. Phys. Chem. A* **2009**, *113*, 9458−9466.

(107) Corey, J. *Chem. Rev.* **2011**, *111*, 863−1071.

(108) Zhang, Q.; Wang, S.; Gu, Y. *J. Phys. Chem. A* **2002**, *106*, 9071−9077.

(109) Zhang, Q.; Gu, Y; Wang, S. *J. Phys. Chem. A* **2003**, *107*, 3884−3890.

(110) Khan, A.; Gossage, R.; Foucher, D. *Can. J. Chem. Rev., Can. Chim.* **2010**, *88*, 1046−1052.

(111) Temelso, B.; Sherrill, C; Merkle, R.; Freitas, R., Jr. *J. Phys. Chem. A* **2007**, *111*, 8677−8688.

(112) Zaleski-Ejgierd, P.; Hoffmann, R.; Ashcroft, N. *Phys. Rev. Lett.* **2011**, *107*, 059902.

(113) Manz, X; Sholl, D. *J. Comput. Chem.* **2010**, *31*, 1528−1541.

(114) Sola, M; Toro-Labbe, A. *J. Phys. Chem. A* **1999**, *103*, 8847.

(115) Toro-Labbe, A. *J. Phys. Chem. A* **1999**, *103*, 4398.

(116) Toro-Labbe, A.; Gutierrez-Oliva, S.; Murray, J.; Politzer, P. *Mol. Phys.* **2007**, *105*, 2619−2625.

(117) Voehringer-Martinez, E.; Toro-Labbe, A. *J. Phys. Chem. A* **2012**, *116*, 7419−7423.